# Preparation of $Y^{3+}$-doped $Bi_2MoO_6$ nanosheets for improved visible-light photocatalytic activity: Increased specific surface area, oxygen vacancy formation and efficient carrier separation

Hong Qiu, Shujing Liu, Xiaohui Ma, Yajie Li, Yueyan Fan, Wenjun Li, and Hualei Zhou

---

## Articles you may be interested in

Rui-qi Yang, Na Liang, Xuan-yu Chen, Long-wei Wang, Guo-xin Song, Yan-chen Ji, Na Ren, Ya-wei Lü, Jian Zhang, and Xin Yu, $Sn/Sn_3O_{4-x}$ heterostructure rich in oxygen vacancies with enhanced visible light photocatalytic oxidation performance, *Int. J. Miner. Metall. Mater.*, 28(2021), No. 1, pp. 150-159. https://doi.org/10.1007/s12613-020-2131-z

Muntadher I. Rahmah, Raad S. Sabry, and Wisam J. Aziz, Preparation and photocatalytic property of $Fe_2O_3$/ZnO composites with superhydrophobicity, *Int. J. Miner. Metall. Mater.*, 28(2021), No. 6, pp. 1072-1079. https://doi.org/10.1007/s12613-020-2096-y

Huan-huan Wang, Wen-xiu Liu, Jing Ma, Qian Liang, Wen Qin, Patrick Osei Lartey, and Xiao-jiang Feng, Design of $(GO/TiO_2)_N$ one-dimensional photonic crystal photocatalysts with improved photocatalytic activity for tetracycline degradation, *Int. J. Miner. Metall. Mater.*, 27(2020), No. 6, pp. 830-839. https://doi.org/10.1007/s12613-019-1923-5

Xiong-feng Zeng, Jian-sheng Wang, Ying-na Zhao, Wen-li Zhang, and Meng-huan Wang, Construction of $TiO_2$-pillared multilayer graphene nanocomposites as efficient photocatalysts for ciprofloxacin degradation, *Int. J. Miner. Metall. Mater.*, 28(2021), No. 3, pp. 503-510. https://doi.org/10.1007/s12613-020-2193-y

Hai-tao Wang, Zi-xiang Wang, Lian-zheng Wang, Jing-qin Wang, and Yan-cai Zhu, Effect of sintering temperature on the physical properties and electrical contact properties of doped $AgSnO_2$ contact materials, *Int. J. Miner. Metall. Mater.*, 25(2018), No. 11, pp. 1275-1285. https://doi.org/10.1007/s12613-018-1680-x

Chun-fa Liao, Yun-fen Jiao, Xu Wang, Bo-qing Cai, Qiang-chao Sun, and Hao Tang, Electrical conductivity optimization of the $Na_3AlF_6$-$Al_2O_3$-$Sm_2O_3$ molten salts system for Al-Sm intermediate binary alloy production, *Int. J. Miner. Metall. Mater.*, 24(2017), No. 9, pp. 1034-1042. https://doi.org/10.1007/s12613-017-1493-3

IJMMM WeChat          QQ author group

# Preparation of $Y^{3+}$-doped $Bi_2MoO_6$ nanosheets for improved visible-light photocatalytic activity: Increased specific surface area, oxygen vacancy formation and efficient carrier separation

*Hong Qiu[1,2],\*, Shujing Liu[3],\*, Xiaohui Ma[1], Yajie Li[1], Yueyan Fan[1], Wenjun Li[1], and Hualei Zhou[1],✉*

1) Department of Chemistry and Chemical Engineering, School of Chemistry and Biological Engineering, University of Science and Technology Beijing, Beijing 100083, China
2) College of Applied Science and Technology, Beijing Union University, Beijing 100012, China
3) BGRIMM MTC Technology Co., Ltd., Beijing 102680, China

**Abstract:** Although $Bi_2MoO_6$ (BMO) has recently received extensive attention, its visible-light photocatalytic activity remains poor due to its limited photoresponse range and low charge separation efficiency. In this work, a series of visible-light-driven $Y^{3+}$-doped BMO (Y-BMO) photocatalysts were synthesized via a hydrothermal method. Degradation experiments on Rhodamine B and Congo red organic pollutants revealed that the optimal degradation rates of Y-BMO were 4.3 and 5.3 times those of pure BMO, respectively. The degradation efficiency of Y-BMO did not significantly decrease after four cycle experiments. As a result of $Y^{3+}$ doping, the crystal structure of BMO changed from a thick layer structure to a thin flower-like structure with an increased specific surface area. X-ray photoelectron spectroscopy showed the presence of high-intensity peaks for the O 1s orbital at 531.01 and 530.06 eV, confirming the formation of oxygen vacancies in Y-BMO. Photoluminescence (PL) and electrochemical impedance spectroscopy measurements revealed that the PL intensity and interface resistances of composites decreased significantly, indicating reduced electron–hole pair recombination. This work provides an effective way to prepare high-efficiency Bi-based photocatalysts by doping rare earth metal ions for improved photocatalytic performance.

**Keywords:** photocatalysts; dye sensitization; bismuth molybdate; yttrium-doped

## 1. Introduction

Photocatalytic degradation is receiving increasing attention with the growing seriousness of environmental problems [1–3]. Efficient photocatalysts are essential for photodegradation. Therefore, developing and studying high-efficiency and low cost photocatalysts for photocatalytic degradation technology is crucial [4–6]. Yu and Kudo [7] first prepared two-dimensional $Bi_2MoO_6$ (BMO) nanosheets with an Aurivillius structure for photocatalysis under the assistance of surfactants. In recent years, BMO has attracted considerable attention in the degradation of organic pollutants given its advantages of low cost, nontoxicity, and narrow band gap [8–10]. However, pure BMO has poor photocatalytic activity due to its fast carrier recombination. Various modification methods, such as metal loading, heterojunction construction, and ion doping, have been explored to enhance the photocatalytic performance of BMOs [11–14]. Ion (Fe and Ni) doping could effectively enhance the photocatalytic activity of BMO [15–16]. Wang *et al.* [17] prepared B-BMO photocatalysts with nonmetal doping. They found that $B^{3+}$ doping led to the generation of $Bi^{5+}$ and oxygen vacancies, which

enhanced light absorption capacity to improve photocatalytic activity. Dutta *et al.* [18] prepared a series of BMO photocatalysts by doping $Mn^{2+}$, $Cu^{2+}$, and $Zn^{2+}$. The photocatalytic performance of all doped BMO photocatalysts in the degradation of organic pollutants in wastewater under visible-light irradiation was significantly enhanced.

Recently, many researchers have focused on modifying semiconductors through rare earth ion doping [19–20]. Xu *et al.* [21] found that doping Eu into $Bi_2WO_6$ could change the morphology of photocatalysts and thus improve photocatalytic activity. Jiang *et al.* [22] testified that for Ce-doped $BiVO_4$, $Ce^{3+}$ could act as hole traps to delay carrier recombination. Xu *et al.* [23] reported on the use of Y-doped $CeO_2$ with small band gaps and oxygen vacancies for the efficient degradation of organic pollutants. Although Y has similar properties as rare earth ions and has great potential in photocatalysis, only a few studies on Y-doped-modified photocatalysts have been conducted. Since $Y^{3+}$ ion (104 pm) has a slightly smaller ionic radius than $Bi^{3+}$ ion (116 pm), the smaller $Y^{3+}$ could replace the $Bi^{3+}$ position. Doping small amounts of Y may improve the light absorption capacity of BMO and increase carrier separation by forming oxygen va-

cancies in BMO to obtain elevated photocatalytic activity. Therefore, Y-doped BMO may also be a good photocatalyst for the photocatalytic degradation of organic pollutants.

Herein, Y³⁺-doped BMO was prepared by using a simple hydrothermal method. A series of characterization tests were performed to explore the influence of Y³⁺ doping on the carrier separation efficiency, obvious morphology, optical capacity, and chemical composition of the synthesized photocatalysts. The photocatalytic degradation performance of Y-BMO in the degradation of Rhodamine B (RhB) and Congo Red (CR) organic pollutants under visible light was investigated. Finally, radical trapping experiments showed that the superoxide radical ($\cdot O_2^-$) and holes play the main roles in degradation. The mechanism of the synergistic induction effect of Y³⁺ doping on morphological changes and oxygen vacancy defects was proposed on the basis of all the results.

## 2. Experimental

### 2.1. Synthesis of BMO and Y³⁺-doped BMO

$Bi(NO_3)_3 \cdot 5H_2O$ (2 mmol) and $(NH_4)_6Mo_7O_{24} \cdot 4H_2O$ (0.14 mmol) were dissolved in $HNO_3$ (2 mol/L) and deionized water, respectively. The two solutions were mixed under continuous stirring. A certain amount of $Y(NO_3)_3$ solution (atomic ratio of Y : Bi = 0.5at%, 1.0at%, 1.5at%, 2.0at%, or 3.0at%) was slowly added to the above solution. Then, the pH of the solution was adjusted to 9 with $NH_3 \cdot H_2O$. After 1 h of stirring, the solution (approximately 80 mL) was kept in a 100 mL Teflon-lined steel autoclave at 180°C for 12 h. After cooling, a light-yellow BMO (Y-BMO) sample was obtained via centrifugation, washing, and drying. The resulting sample was recorded as $x$Y-BMO ($x$ is 0.5, 1.0, 1.5, 2.0, or 3.0). Through the same method, pure BMO (BMO) was prepared without the addition of $Y(NO_3)_3$.

### 2.2. Characterization

The phase structure of the prepared samples was determined through X-ray diffraction (XRD, D/Max RB, Rigaku, Japan) and X-ray photoelectron spectroscopy (XPS, ESCAL-AB 250Xi, Thermo Fisher, USA). The morphology of the photocatalysts was detected by scanning electron microscopy (SEM, S-4800; Hitachi, Japan) and high-resolution

transmission electron microscopy (HRTEM, F-20, FEI, USA). The light absorption properties and photoluminescence (PL) spectra of the samples were recorded by an ultraviolet–visible (UV–Vis) spectrophotometer (T9s, Persee, China) and fluorescence spectrophotometer (F-4500, Hitachi, Japan), respectively.

### 2.3. Photocatalytic degradation experiment

The photocatalytic activity of the synthesized samples in the degradation of RhB (20 mg/L) and CR (20 mg/L) was evaluated under 400 W Xenon lamp illumination ($\lambda > 420$ nm). First, 30 mg of the photocatalyst was dispersed in 30 mL of RhB or CR solution under strong agitation. The solution was stirred in the dark for 2 h to achieve adsorption–desorption equilibrium. A total of 3 mL of solution was acquired at a certain time point and then centrifuged to eliminate solid residue. Subsequently, the concentrations of CR and RhB were tested by using a UV–Vis spectrophotometer (T9s, Persee, China) at 496 and 553 nm, respectively. The degradation ratio ($C/C_0$) was used to assess photocatalytic activity ($C$: concentration at a certain time; $C_0$: incipient concentration).

### 2.4. Electrochemical measurements

Electrochemical impedance measurement was performed by using a three-electrode workstation. A calomel electrode, platinum wire, and conductive glass (sample prepared by surface coating) were used as the reference, auxiliary, and working electrodes, respectively. A 3 mg sample was homogeneously dispersed in an appropriate amount of ethanol by ultrasound. Then, the suspension was uniformly coated onto indium tin oxide conductive glass with a diameter of 6 mm. $Na_2SO_4$ (0.5 mol·L⁻¹) was used as an electrolyte.

## 3. Results and discussion

### 3.1. Structural analysis

Fig. 1 illustrates the XRD spectra of all samples. Fig. 1(a) shows that BMO (JCPDS Card No. 21-0102) has ten very typical diffraction peaks at 10.9°, 28.2°, 32.5°, 33.1°, 46.7°, 47.1°, 55.4°, and 56.6° that correspond to the (020), (131), (200), (060), (202), (260), (331), and (191) crystal planes, re-
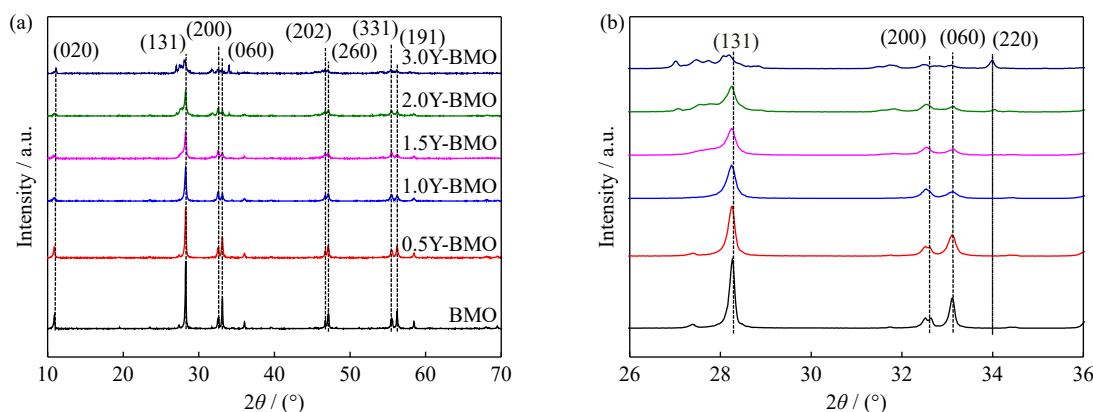


**Fig. 1.** (a) XRD patterns of the pure Bi₂MoO₆ (BMO) and Y³⁺-doped BMO (Y-BMO) samples; (b) comparative analysis of (131), (200), (060), and (220) in the XRD patterns of the pure BMO and Y-BMO samples.

1826

*Int. J. Miner. Metall. Mater., Vol. 30, No. 9, Sep. 2023*

spectively. However, finding the diffraction peaks of Y in Y-BMO samples is difficult due to the low Y content. Diffraction peak intensity is mainly related to the crystallinity of the samples, and ion doping could reduce crystallinity. Compared with that of BMO, the diffraction peak intensity of Y-BMO samples has decreased visibly, demonstrating that $Y^{3+}$ doping reduced the order degree of cations. This phenomenon also indicates that $Y^{3+}$ has successfully replaced $Bi^{3+}$ in the BMO lattice [24]. Fig. 1(b) presents that for all samples, the crystal planes at 28.3°, 32.5°, 33.1°, and 34.5° have shifted. The diffraction peaks tend to shift to low angles, indicating that $Y^{3+}$ is incorporated into the crystal and causes lattice expansion [25]. Moreover, in contrast to the weakened peak intensity of the (131), (200), and (060) crystal planes, the peak intensity of the (220) crystal plane at 34.5° has increased, indicating that the crystal phase may preferentially grow in the

[110] direction after $Y^{3+}$ doping.

To further explore the change in the crystal phase, the crystal parameters of Y-BMO and pure BMO were estimated in accordance with the XRD crystal data (Table 1). The cell parameters of the Y-BMO samples gradually increase with the increase in Y content, likely due to the distortion of the octahedral $MoO_6$ structure and the shifting of the oxygen atoms in the top $(Bi_2O_2)_n^{2+}$ layer [26–28]. Simultaneously, the XRD analysis shows that after Y doping, the crystal phase of BMO does not change. The radius of $Y^{3+}$ (104 pm) is smaller than that of $Bi^{3+}$ (116 pm), and the smaller $Y^{3+}$ could replace the $Bi^{3+}$ position of the BMO. In accordance with Vegard's law [29] and as confirmed by the experimental results, the lattice volume of the Y-BMO samples should be between the lattice volumes of BMO (0.488683 $nm^3$) and $Y_2MoO_6$ (0.913900 $nm^3$) [30].

**Table 1.  Crystal parameters of the Y-BMO and pure BMO samples**

| Sample | Lattice parameters | | | Lattice volume, $V$ / $nm^3$ |
|---|---|---|---|---|
| | $a$ / nm | $b$ / nm | $c$ / nm | |
| Pure BMO | 0.5502 | 1.6199 | 0.5483 | 0.488683 |
| 0.5Y-BMO | 0.5502 | 1.6213 | 0.5483 | 0.489105 |
| 1.0Y-BMO | 0.5506 | 1.6226 | 0.5487 | 0.490211 |
| 1.5Y-BMO | 0.5506 | 1.6227 | 0.5488 | 0.490330 |
| 2.0Y-BMO | 0.5509 | 1.6227 | 0.5490 | 0.490776 |
| 3.0Y-BMO | 0.5513 | 1.6240 | 0.5490 | 0.491526 |
| $Y_2MoO_6$ | 1.6350 | 1.1019 | 0.5349 | 0.913900 |

### 3.2. Morphological characterization

SEM, TEM, and HRTEM were applied to further explore the effect of $Y^{3+}$ doping on the micromorphology of BMO. Fig. 2 shows the SEM images of pure BMO and 1.5Y-BMO. The synthesized BMO presents an irregular thick layer with uneven size and good dispersion. After $Y^{3+}$ doping, the layer-like sample has obviously thinned and shows flower-like agglomeration. Fig. 2(c) shows that compared with that of BMO, the specific surface area of the flower-like 1.5Y-BMO has significantly increased. This increase may improve photocatalytic activity. Fig. 3 exhibits the TEM and HRTEM images of the BMO and 1.5Y-BMO samples. Both samples have obvious diffraction spots. Nevertheless, the 1.5Y-BMO sample has a thinner lamella than the pure BMO. The lattice spacings of pure BMO are 0.275, 0.274, and 0.260 nm, which correspond to the (002), (200), and (220) crystal planes of BMO, respectively. Compared with those in the BMO

sample, all lattice fringes have increased, and the diffraction fringes of the (220) crystal plane are more obvious in the 1.5Y-BMO sample. The aforementioned results and XRD results confirm that doping $Y^{3+}$ into the BMO lattice causes lattice deformation. Growth occurs in the [110] direction when the doping amount reaches a certain level, thus making the crystal morphology change from a thick sheet into a flower-like structure. HRTEM results suggest that the lattice volume of doped samples increases due to the special effect of the dominant growth direction in the BMO lattice after $Y^{3+}$ doping [10,31–33]. Meanwhile, the TEM mapping results also prove that Y has been successfully incorporated (Fig. 4).

### 3.3. XPS analysis

The XPS results of 1.5Y-BMO were studied. Fig. 5(a) shows that the spectra of the 1.5Y-BMO samples exhibit Bi, Mo, O, and Y signals. As shown in Fig. 5(b), the peaks loc-
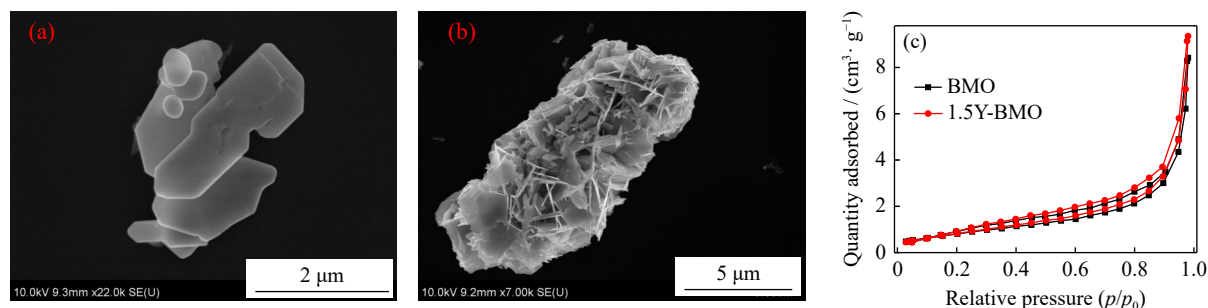


**Fig. 2.  SEM images of pure BMO (a) and 1.5Y-BMO (b) and the $N_2$ adsorption–desorption isotherm (c) of BMO and 1.5Y-BMO.**
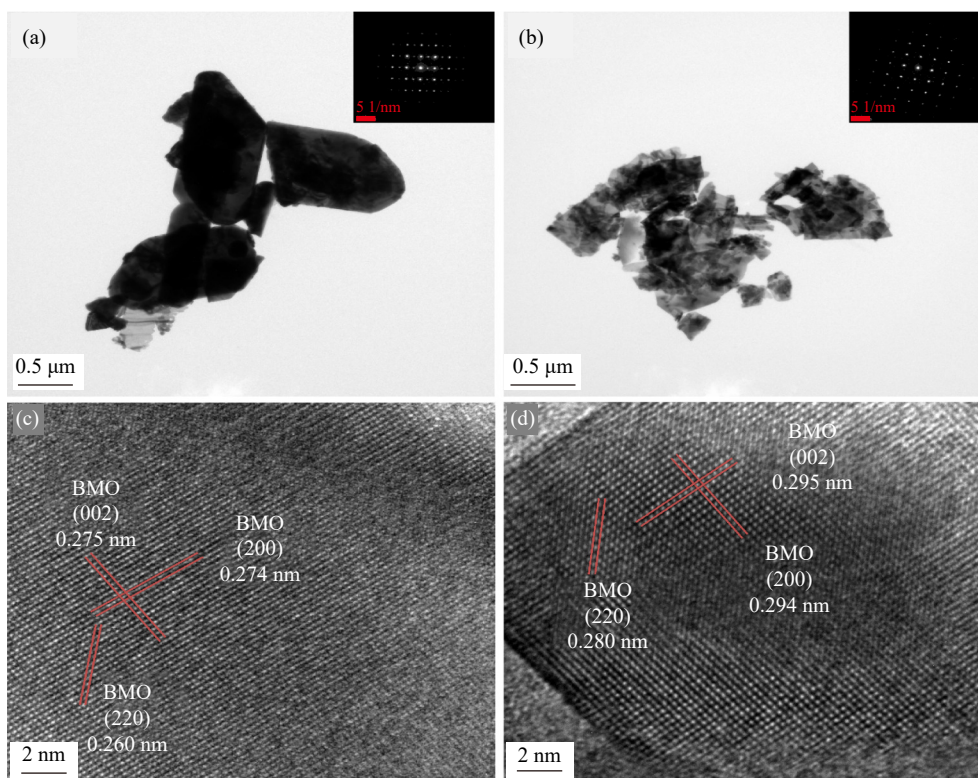
**Fig. 3.** TEM and HRTEM images of pure BMO (a, c) and 1.5Y-BMO (b, d). The insets in (a) and (b) are the corresponding diffraction spots.
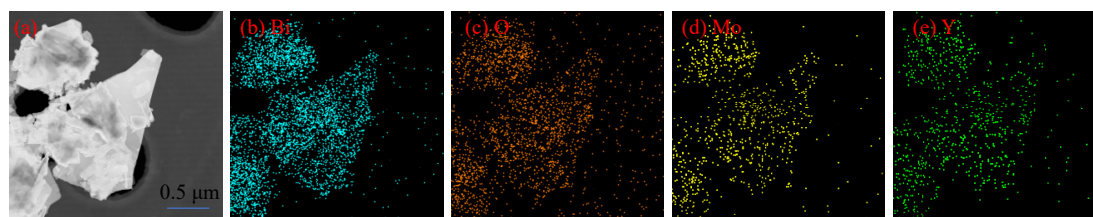


**Fig. 4.** TEM image maps of 1.5Y-BMO: (a) TEM image of 1.5Y-BMO; (b) Bi; (c) O; (d) Mo; (e) Y.

ated at 164.1 and 158.9 eV belong to Bi 4f$_{5/2}$ and Bi 4f$_{7/2}$, respectively, and are allocated to Bi$^{3+}$ [34]. Fig. 5(c) shows the high-resolution Mo 3d XPS spectra of 1.5Y-BMO samples. The signal peaks at 232.3 and 235.4 eV belong to Mo 3d$_{5/2}$ and Mo 3d$_{3/2}$ of Mo(VI), respectively [35]. In Fig. 5(d), the O 1s intensity peaks at 530.1 and 531.0 eV belong to the oxygen vacancies anion and O$^{2-}$ of 1.5Y-BMO [36]. The formation of vacancies could result from the distortion of the octahedral MoO$_6$ structure and the induction of local electric charge imbalance [37]. In Fig. 5(e), the peaks located at 164.4 and 159.1 eV belong to Y 3d$_{3/2}$ and Y 3d$_{5/2}$ [38], respectively. The absence of a diffraction peak at 156.8 eV for the 3d$_{5/2}$ of Y$^{3+}$ [39] indicates that Y$^{3+}$ has been doped into the lattice through Bi–O–Y formation [28]. These results are indicative of the successful preparation of Y-BMO and the presence of oxygen vacancies in Y-BMO materials, which would contribute to the improvement in photocatalytic performance.

### 3.4. Optical properties

The optical properties of the BMO and Y-BMO samples were studied by using the diffuse reflection spectrum technique [40]. Fig. 6(a) shows that the incorporation of Y$^{3+}$ has greatly broadened the light absorption range of BMO. The edge in Y-BMO has distinctly right-shifted relative to that in pure BMO. With the increase in Y content, the light response range of the Y-BMO sample has gradually expanded. This finding indicates that Y$^{3+}$ doping could effectively improve the light absorption performance of semiconductor materials. The band gap energy ($E_g$) values of all samples could be estimated by using the Kubelka–Munk equation:

$$Ah\nu = \alpha(h\nu - E_g)^{\frac{n}{2}},$$

where $A$, $h$, $\nu$, $\alpha$, and $E_g$ represent the absorption coefficient, Planck constant, optical frequency, ratio, and optical energy gap value of the light absorption edge, respectively. The value of n is 1 or 4. The $E_g$ of pure BMO, 0.5Y-BMO, 1.0Y-BMO, 1.5Y-BMO, 2.0Y-BMO, and 3.0Y-BMO samples are 2.72, 2.70, 2.68, 2.65, 2.62, and 2.52 eV, respectively. The Y dopant could narrow the band gap of BMO due to the introduction of impurity levels [41–43]. These results suggest that the introduction of Y$^{3+}$ into the BMO crystal lattice could increase light absorption, thus enhancing photocatalytic degradation efficiency.

1828

*Int. J. Miner. Metall. Mater., Vol. 30, No. 9, Sep. 2023*
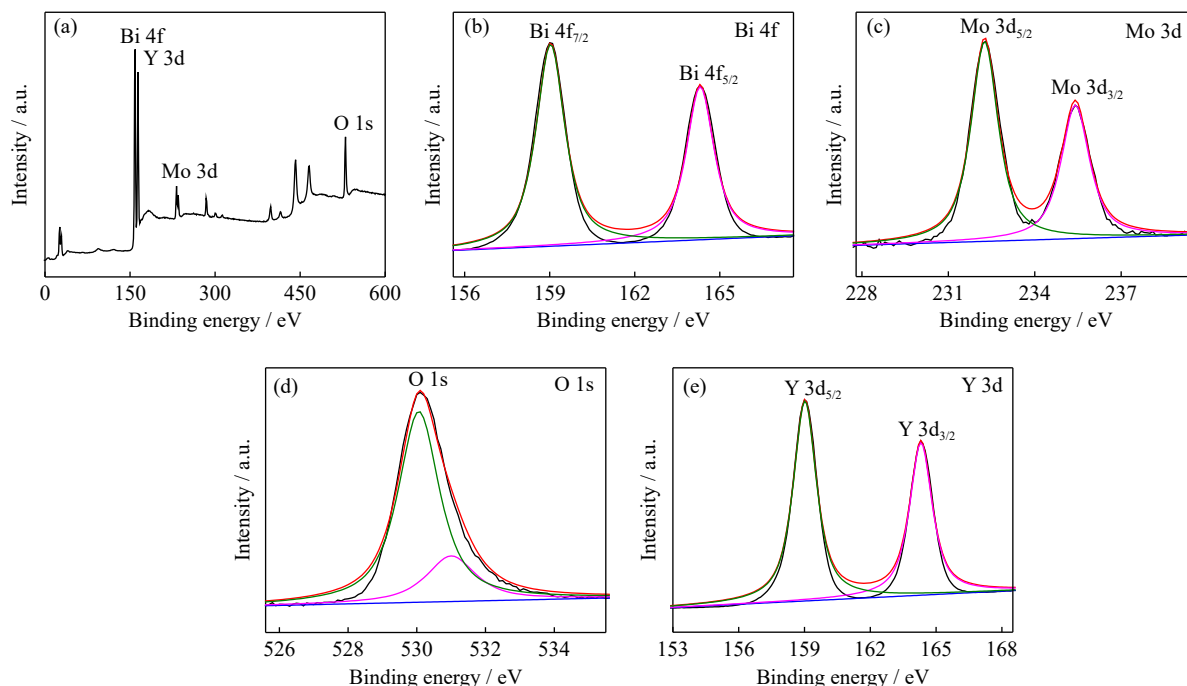


**Fig. 5.   XPS spectra of 1.5Y-BMO: (a) full spectrum; (b) Bi 4f; (c) Mo 3d; (d) O 1s; (e) Y 3d.**
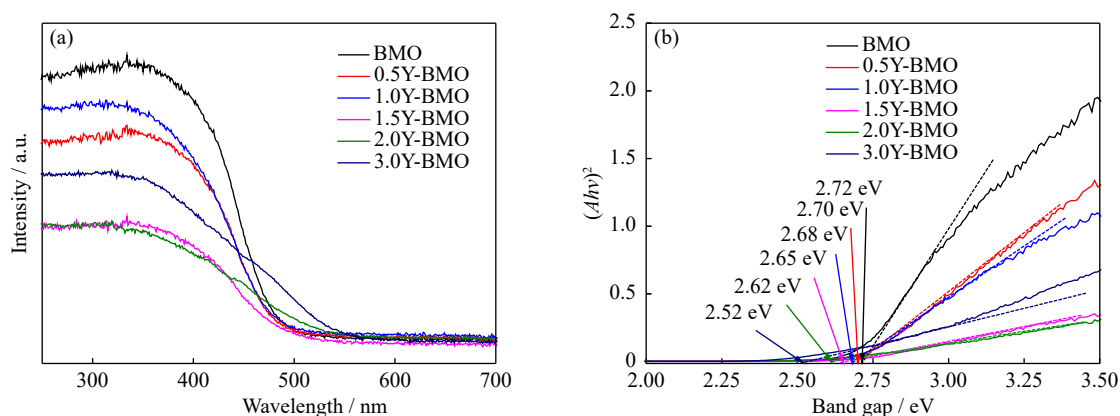


**Fig. 6.   (a) DRS spectra of pure BMO and Y-BMO samples; (b) band gap energies of the corresponding photocatalysts.**

### 3.5. Photocatalytic tests

The photocatalytic performance of the synthesized samples in the degradation of RhB and CR under visible light was tested. Before the photodegradation experiment, the samples were dispersed in the pollutant solution in the dark for 2 h to achieve adsorption–desorption equilibrium. Fig. 7(a) shows the RhB photocatalytic degradation performance of the pure BMO and Y-BMO photocatalysts. All $Y^{3+}$-doped Y-BMO samples show significantly improved photocatalytic activity. Among these samples, 1.5Y-BMO has the best photocatalytic degradation performance. After 90 min, 1.5Y-BMO has degraded more than 94% of RhB organic pollutants. The degradation efficiency of 1.5Y-BMO is 4.3 times that of pure BMO samples (22%). When the doping amount of $Y^{3+}$ exceeds 1.5at%, photocatalytic performance decreases, likely because the additional $Y^{3+}$ ions have become the composite center of photogenerated carriers, and the band gap of Y-BMO has narrowed. The following reaction kinetics model was used to analyze the RhB photode-

gradation reaction of Y-BMO:

$$\ln(C_0/C) = kt,$$

where $C_0$ is the initial concentration of the RhB solution in the dark, $k$ is the apparent velocity constant, and $C$ is the concentration at a certain time. As shown in Fig. 7(b), the $k$ values of pure BMO, 0.5Y-BMO, 1.0Y-BMO, 1.5Y-BMO, 2.0Y-BMO, and 3.0Y-BMO are 0.0032, 0.0196, 0.0227, 0.0297, 0.0250, and 0.0210 $min^{-1}$, respectively. The photocatalytic reaction rates of all photocatalysts are significantly higher than those of BMO, and the photodegradation reaction rate of the 1.5Y-BMO samples is the highest. The above results completely demonstrate that $Y^{3+}$-doped BMO is an efficient photocatalyst. The degradation of CR was also studied to further explore the photocatalytic performance of the samples. The photodegradation process of CR was the same as that of RhB. As inferred from Fig. 7(c), the degradation efficiency of the series of Y-BMO materials is significantly higher than that of BMO. 1.5Y-BMO shows the maximum degradation efficiency (above 85%) after 150 min un-
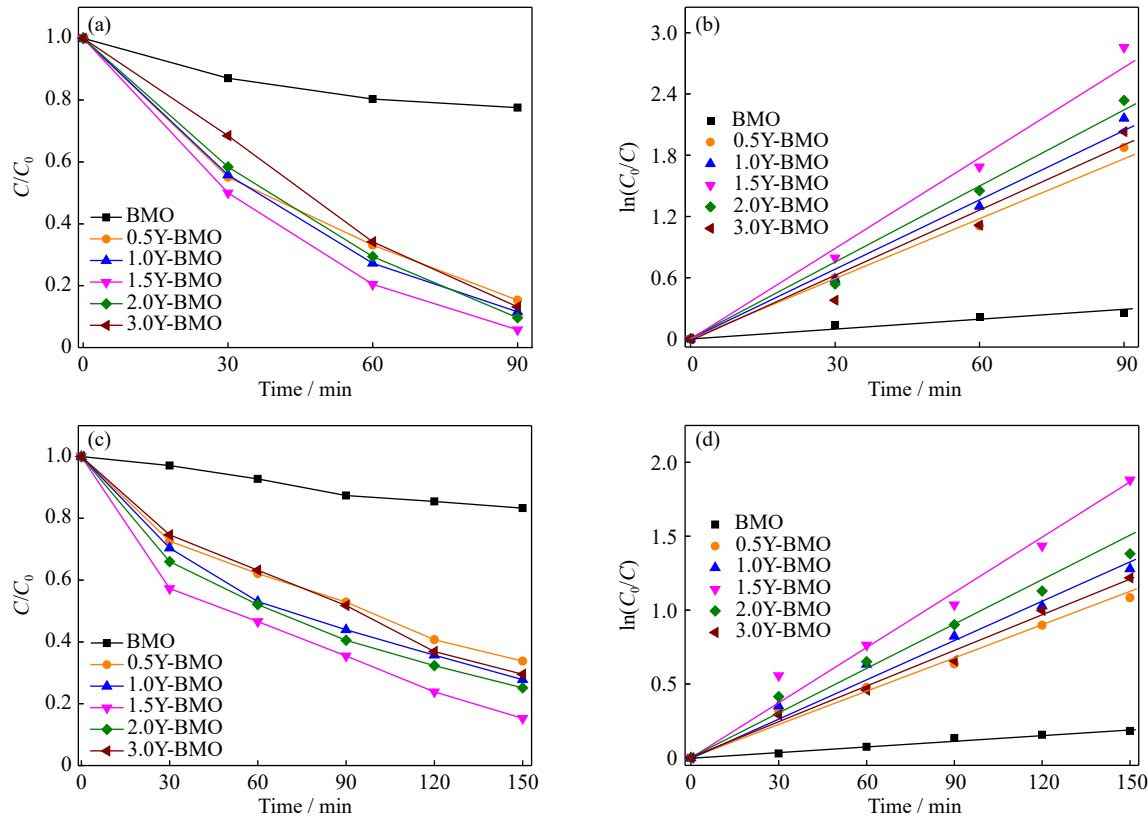
**Fig. 7.    RhB (a, b) and CR (c, d) degradation ratio and degradation kinetics curves of pure BMO and Y-BMO samples.**

der visible-light. The maximum degradation efficiency of 1.5Y-BMO is equivalent to 5.3 times the degradation efficiency (16%) of pure BMO samples. Similarly, the $k$ values of pure BMO, 0.5Y-BMO, 1.0Y-BMO, 1.5Y-BMO, 2.0Y-BMO, and 3.0Y-BMO are 0.0012, 0.0075, 0.0088, 0.0124, 0.0101, and 0.0081 min⁻¹, respectively. The experimental results show that Y-BMO materials have good photocatalyt-

ic activity and could effectively degrade different organic pollutants and dyes in a short time.

Photocatalyst stability is an important evaluation index in environmental treatment applications. 1.5Y-BMO was used to degrade RhB to evaluate the stability of the photocatalysts (Fig. 8(a)). After four photodegradation cycle experiments, the photocatalytic activity of 1.5Y-BMO remains above
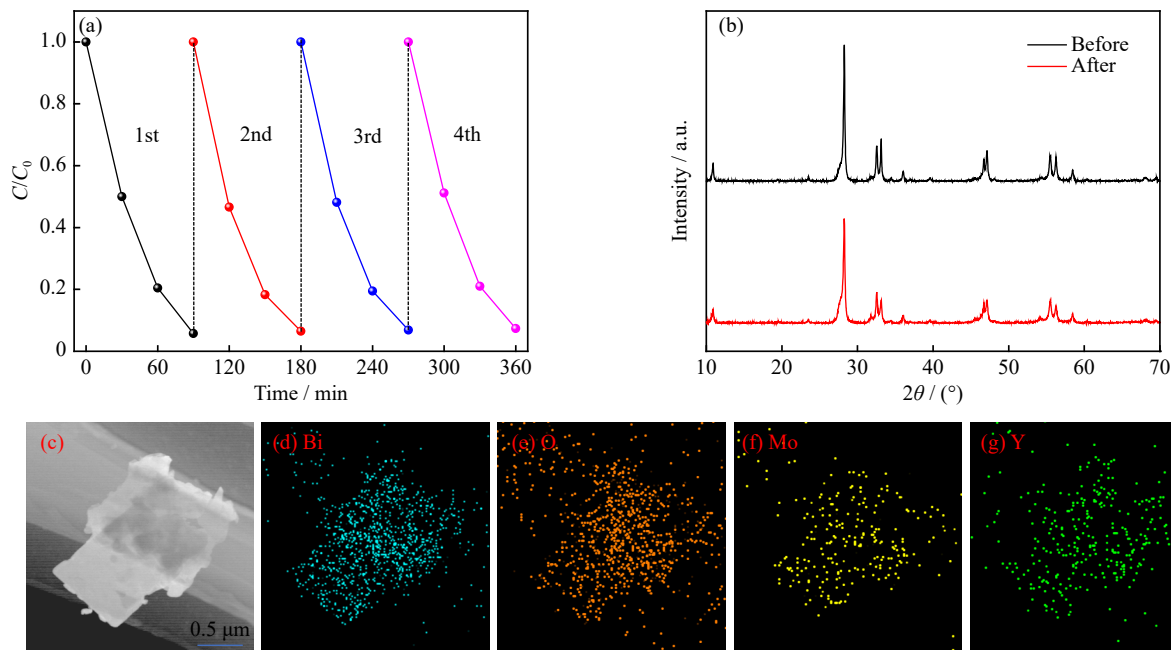


**Fig. 8.    (a) RhB photocatalytic degradation cycle of 1.5Y-BMO; (b) XRD pattern of the 1.5Y-BMO samples before and after photo-degradation; (c–g) Mapping of the TEM images of 1.5Y-BMO after photodegradation: (c) TEM image of 1.5Y-BMO, (d) Bi, (e) O, (f) Mo, and (g) Y.**

92%. The slight reduction in photocatalytic efficiency may be due to the loss of the photocatalyst during recovery. In addition, the XRD patterns of 1.5Y-BMO before and after photocatalytic degradation have not obviously changed, as shown in Fig. 8(b), indicating that the photodegradation process will not affect the crystal structure of the doped materials. The TEM elemental mapping (Fig. 8(c)–(g)) and XPS

(Fig. 9) of the samples after photodegradation were studied to confirm the stable existence of the Y dopant within the BMO lattice. The results definitely show the stable existence of Y in BMO, which is in accordance with the XRD results. The above results prove that the Y-BMO material has good chemical stability during photodegradation. Therefore, Y-BMO should be a potential visible-light photocatalyst.
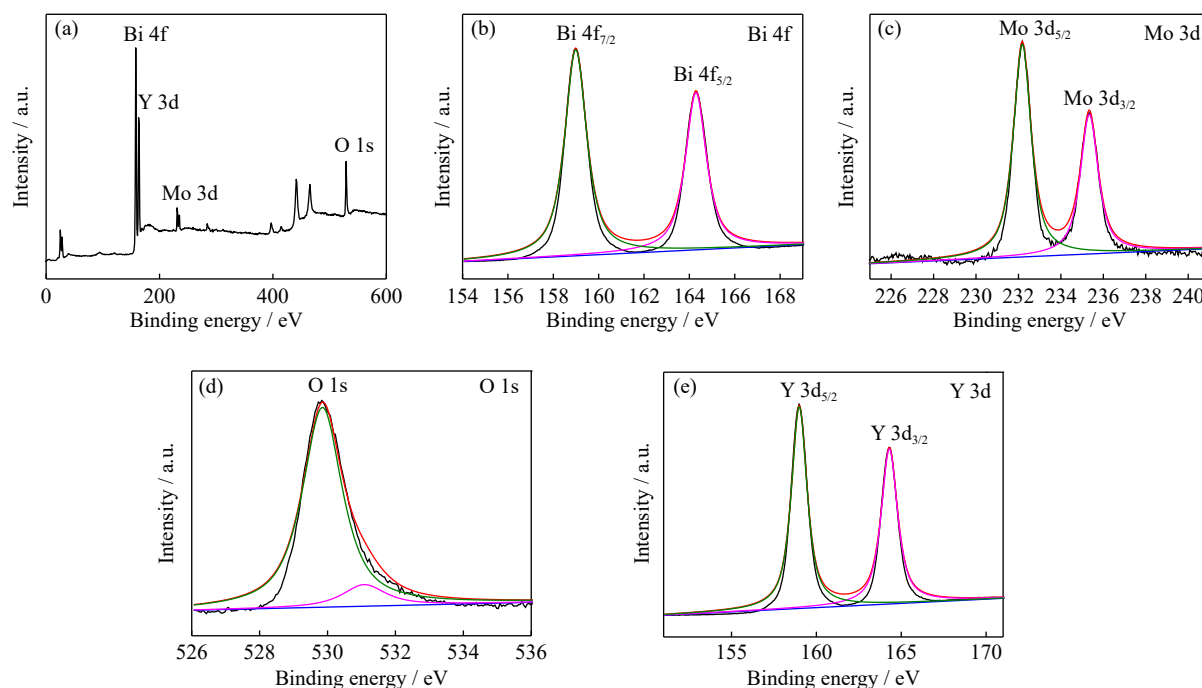


**Fig. 9.    XPS spectra of 1.5Y-BMO after photodegradation: (a) full spectrum; (b) Bi 4f; (c) Mo 3d; (d) O 1s; (e) Y 3d.**

## 3.6. Photocatalytic mechanism

The above experiments showed that the Y-BMO photocatalysts could significantly improve visible-light catalytic activity. The PL and EIS spectra of the synthesized photocatalysts were acquired to further explore the mechanism

underlying the enhancement in photocatalytic performance [44–45]. As shown in Fig. 10(a), all samples have evident PL signals at 470 nm. After $Y^{3+}$ doping, the PL intensities of the Y-BMO photocatalysts have reduced compared with those of pure BMO, indicating that the carrier separation efficiency of
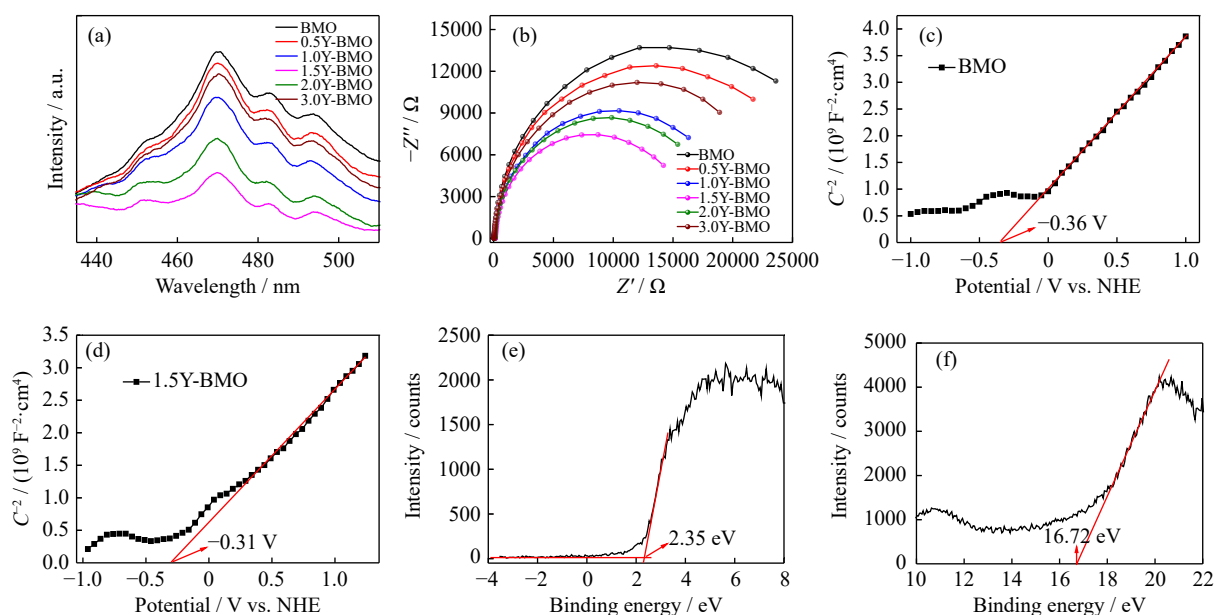


**Fig. 10.    PL (a) and EIS (b) spectra of pure BMO and the Y-BMO samples; Mott–Schottky plots of pure BMO (c) and 1.5Y-BMO (d); the valence band XPS (e) and cutoff energy region (f) of BMO.**

Y-BMO has significantly improved. In addition, in complete line with the order of photocatalytic pollutant degradation efficiency, the order of the PL intensities of all synthetic samples is BMO > 0.5Y-BMO > 3.0Y-BMO > 1.0Y-BMO > 2.0Y-BMO > 1.5Y-BMO. Among the samples, 1.5Y-BMO has the lowest PL peak intensity, indicating that it has the highest carrier separation efficiency. The PL peak intensities of Y-BMO enhance when the doped Y³⁺ content exceeds 1.5at%, likely because the excessive doping of Y³⁺ results in the narrowing of the band gap of Y-BMO. The smaller the radius of the Nyquist plot arc, the smaller the resistance of charge transfer [46-47]. In Fig. 10(b), compared with those of pure BMO samples, the radii of Y-BMO series samples have significantly reduced. The radius of the 1.5Y-BMO sample is the smallest. The aforementioned results indicate that the doping of Y³⁺ could greatly promote the migration and separation of photoexcited carriers in Y-BMO, likely due to the presence of oxygen vacancies that could capture photogenerated electrons in Y-BMO and prolong carrier lifetime [48].

Mott–Schottky and valence band XPS measurements were performed to confirm the band alignment of pure and Y-doped BMO. First, the flat bands of pure and Y-doped BMO were determined by using Mott–Schottky measurements. The positive slope of the linear plot illustrates that pure and Y-doped BMO are n-type semiconductors. Thus, the conduction bands ($E_{CB}$) of pure and Y-doped BMO are approximately equal to their flat bands and are −0.36 and −0.31 V, respectively (Fig. 10(c) and (d)). The valence bands ($E_{VB}$) of pure and 1.5Y-BMO are calculated as 2.36 and 2.34 V, respectively, in accordance with the following formula:

$$E_g = E_{VB} - E_{CB}.$$

The valence band XPS spectrum of pure BMO was studied to confirm the $E_{VB}$ of BMO. Fig. 10(e) and (f) shows that the valence band XPS (VB$_{XPS}$) and secondary electron cutoff energies ($E_{cutoff}$) of BMO are 2.35 and 16.72 eV, respectively. The $E_{VB}$ of BMO is speculated to be 2.39 V [49], which is almost consistent with our Mott–Schottky results (2.36 V) within the error range.

To demonstrate the presence of oxygen vacancies in Y-doped BMO, we carried out electron paramagnetic resonance (EPR) experiments (Fig. 11(a)). In contrast to pure BMO, 1.5Y-BMO has an obvious typical signal peak, indicating that 1.5Y-BMO has more oxygen vacancies than pure BMO [50–54]. This finding also corroborates the above XPS results. After Y³⁺ doping, the octahedral MoO₆ structure has become distorted, which would induce a local electric field inside BMO crystals and oxygen vacancy formation. Consequently, an oxygen vacancy energy level should form in the band gap.

Active species play an important role in photodegradation experiments. In the photodegradation RhB system, isopropanol (IPA, 10 mmol·L⁻¹), benzoquinone (BQ, 1 mmol·L⁻¹), and sodium oxalate (Na₂C₂O₄, 10 mmol·L⁻¹) are used as trapping agents to capture hydroxyl radicals (·OH), ·O₂⁻, and holes, respectively [31,55]. Fig. 11(b) shows that the photocatalytic activity of pure BMO is significantly inhibited by the addition of BQ and Na₂C₂O₄ but is not obviously affected by the addition of IPA. The above results show that ·O₂⁻ and holes play the main role in the degradation process. In the 1.5Y-BMO system, holes and ·O₂⁻ are also the main active species. ·OH is not formed during photocatalytic degradation. The aforementioned results suggest that the doping of Y³⁺ does not alter the active species produced during photodegradation by BMO.

The above discussion shows that the morphology of BMO changes, and BMO grows preferentially in the [110] direction due to Y³⁺ doping. This effect is beneficial to increasing the surface area and surface-active sites of the photocatalyst. Meanwhile, Y³⁺ doping leads to the formation of oxygen vacancy defects in BMO. This phenomenon could expand the visible-light absorption range and improve the separation efficiency of photogenerated carriers. Therefore, we propose the possible photodegradation mechanism of Y-BMO. Fig. 12 shows that the position of the energy level of the oxygen vacancies in Y-BMO should be below and close to the conduction band (0.07 eV). Upon excitation by visible light, electrons could migrate from the valence band of BMO to the conduction band. Nonetheless, additional electrons could migrate from the valence band of BMO to the oxygen vacancy level due to the low energy required for transition. Oxygen vacancy defects can adsorb O₂ on the catalyst surface, and electrons in the oxygen vacancy level can react with O₂ in a
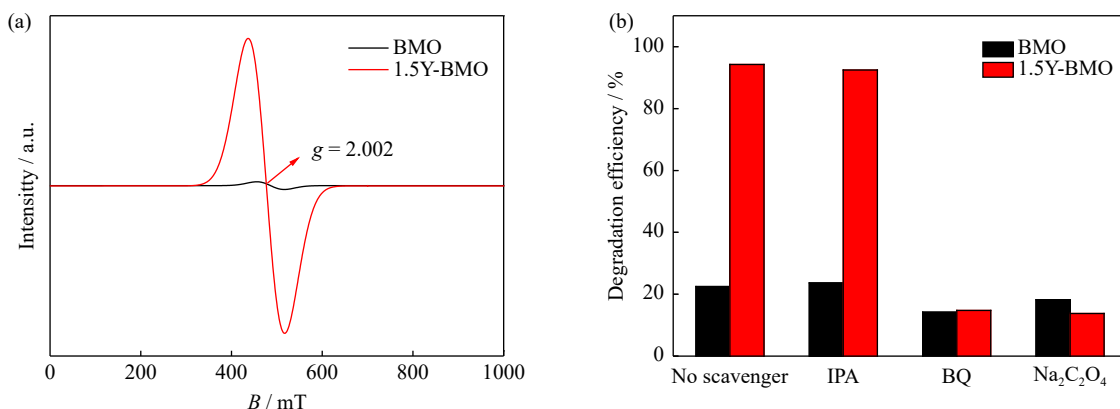


**Fig. 11.** (a) EPR of BMO and 1.5Y-BMO (*B*—Magnetic induction intensity; *g*—Landé *g*-factor); (b) photocatalytic degradation of RhB over BMO and 1.5Y-BMO with the addition of the scavengers IPA, BQ, and Na₂C₂O₄.
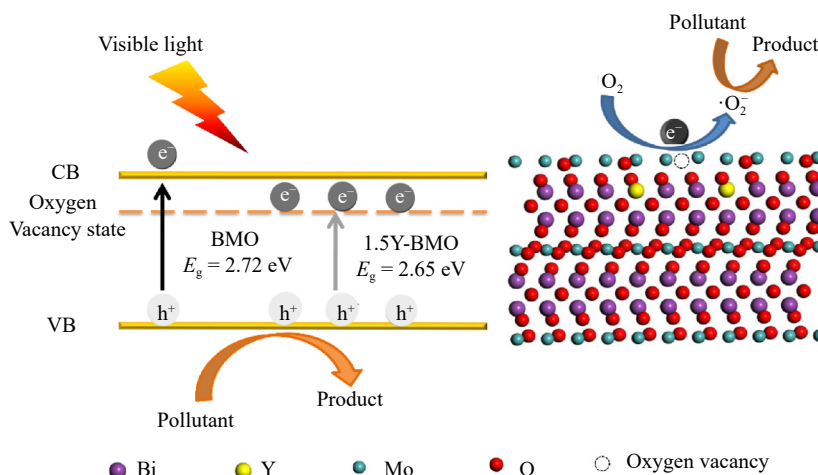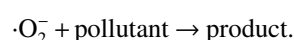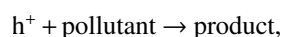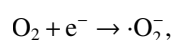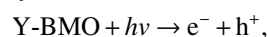
**Fig. 12.    Illustration of the mechanism of organic photodegradation by Y-BMO.**

timely manner to generate $\cdot O_2^-$, thus inhibiting photogenerated carrier recombination. This situation improves the utilization rate of photogenerated electrons and holes, increases the production of $\cdot O_2^-$, and retains more effective holes in the valence band. The created $\cdot O_2^-$ and holes in Y-BMO can directly participate in the degradation of organic pollutants and thus confer excellent photodegradation properties. The free radical photocatalytic degradation of the Y-BMO photocatalyst is

$$Y\text{-}BMO + h\nu \rightarrow e^- + h^+,$$

$$O_2 + e^- \rightarrow \cdot O_2^-,$$

$$h^+ + \text{pollutant} \rightarrow \text{product},$$

$$\cdot O_2^- + \text{pollutant} \rightarrow \text{product}.$$

## 4. Conclusions

A series of novel Y-BMO photocatalysts were prepared through the hydrothermal method. In contrast to BMO, Y-BMO possesses high RhB and CR degradation efficiency. Among Y-BMO photocatalysts, the 1.5Y-BMO samples exhibit the best degradation efficiency under visible-light. The results of this work show that $Y^{3+}$ doping has numerous effects: (1) BMO preferentially grows in the [110] direction, and its microstructure changes from a thick sheet into a flower-like structure with increased specific surface area. (2) After $Y^{3+}$ doping, the formed oxygen vacancy defects improve the carrier separation efficiency of the semiconductor to produce additional active substances for organic pollutant photodegradation. The possible photocatalytic degradation mechanism of Y-BMO was proposed after systematic studies. This study provides an effective strategy for modifying Bi-based photocatalysts through doping rare earth metal ions to obtain high-efficiency photocatalytic performance.

## Acknowledgement

## Conflict of Interest

The authors declare no competing financial interest.

## References

[1]  K.L. Xie, J.F. Fang, L. Li, J.P. Deng, and F.F. Chen, Progress of graphite carbon nitride with different dimensions in the photocatalytic degradation of dyes: A review, *J. Alloys Compd.*, 901(2022), art. No. 163589.

[2]  V.H. Komal Poonia, Pardeep Singh, Aftab Aslam Parwaz Khan, *et al.*, Photocatalytic degradation aspects of atrazine in water: Enhancement strategies and mechanistic insights, *J. Clean. Prod.*, 367(2022), p. 133087.

[3]  C. Liu, S. Mao, M.X. Shi, *et al.*, Enhanced photocatalytic degradation performance of BiVO$_4$/BiOBr through combining Fermi level alteration and oxygen defect engineering, *Chem. Eng. J.*, 449(2022), art. No. 137757.

[4]  M. Hussein Abdurahman, A. Zuhairi Abdullah, W. da Oh, *et al.*, Tunable band structure of synthesized carbon dots modified graphitic carbon nitride/bismuth oxychlorobromide heterojunction for photocatalytic degradation of tetracycline in water, *J. Colloid Interface Sci.*, 629(2023), p. 189.

[5]  S.Y. Liu, A. Zada, X.Y. Yu, F.Z. Liu, and G. Jin, NiFe$_2$O$_4$/g-C$_3$N$_4$ heterostructure with an enhanced ability for photocatalytic degradation of tetracycline hydrochloride and antibacterial performance, *Chemosphere*, 307(2022), art. No. 135717.

[6]  X. Liu, J. Xu, T.T. Zhang, *et al.*, Construction of Ag nanocluster-modified Ag$_3$PO$_4$ containing silver vacancies via *in-situ* reduction: With enhancing the photocatalytic degradation activity of sulfamethoxazole, *J. Colloid Interface Sci.*, 629(2023), p. 989.

[7]  J.Q. Yu and A. Kudo, Hydrothermal synthesis and photocatalytic property of 2-dimensional bismuth molybdate nanoplates, *Chem. Lett.*, 34(2005), No. 11, p. 1528.

[8]  L.J. Xie, J.F. Ma, and G.J. Xu, Preparation of a novel Bi$_2$MoO$_6$ flake-like nanophotocatalyst by molten salt method and evaluation for photocatalytic decomposition of rhodamine B, *Mater. Chem. Phys.*, 110(2008), No. 2-3, p. 197.

[9]  H.D. Li, W.J. Li, F.Z. Wang, X.T. Liu, C.J. Ren, and X. Miao, Fabrication of Pt nanoparticles decorated Gd-doped Bi$_2$MoO$_6$ nanosheets: Design, radicals regulating and mechanism of Gd/Pt-Bi$_2$MoO$_6$ photocatalyst, *Appl. Surf. Sci.*, 427(2018), p. 1046.

[10]  H.D. Li, W.J. Li, S.N. Gu, *et al.*, Enhancement of photocatalytic activity in Tb/Eu co-doped Bi$_2$MoO$_6$: The synergistic effect

of Tb–Eu redox cycles, *RSC Adv.*, 6(2016), No. 53, p. 48089.

[11] C.T. Zou, Z.Y. Yang, M.J. Liang, Y.P. He, Y. Yang, and S.J. Yang, Preparation of Bi/Bi₂MoO₆ plasmonic photocatalyst with high photocatalytic activity under visible light irradiation, *Nano*, 13(2018), No. 11, art. No. 1850127.

[12] H.N. Wei, F.M. Meng, J.L. Li, W.Q. Yu, and H. Zhang, FeIn₂S₄/Bi₂MoO₆ Z-scheme heterostructural composites efficiently degrade tetracycline hydrochloride under visible light, *Appl. Surf. Sci.*, 611(2023), art. No. 155642.

[13] R.F. Chen, W. Zhou, W.W. Qu, Y.J. Wang, L.Y. Shi, and S.M. Chen, A novel hierarchical nanostructured S-scheme RGO/Bi₂MoO₆/Bi₂WO₆ heterojunction: Excellent photocatalytic degradation activity for pollutants, *Appl. Surf. Sci.*, 588(2022), art. No. 152788.

[14] Z.X. Yang, R.Q. Wang, L.J. Xu, *et al.*, Highly efficient flower-like Dy³⁺-doped Bi₂MoO₆ photocatalyst under simulated sunlight: Design, fabrication and characterization, *Opt. Mater.*, 116(2021), art. No. 111094.

[15] L. Yang, C.Y. Du, S.Y. Tan, *et al.*, L. Zhou, and J. Chen, Improved photocatalytic properties of Fe(III) ion doped Bi₂MoO₆ for the oxidation of organic pollutants, *Ceram. Int.*, 47(2021), No. 4, p. 5786.

[16] J. Wang, Y.G. Sun, C.C. Wu, Z. Cui, and P.H. Rao, Enhancing photocatalytic activity of Bi₂MoO₆ via surface co-doping with Ni²⁺ and Ti⁴⁺ ions, *J. Phys. Chem. Solids*, 129(2019), p. 209.

[17] M. Wang, J. Han, P.Y. Guo, *et al.*, Hydrothermal synthesis of B-doped Bi₂MoO₆ and its high photocatalytic performance for the degradation of Rhodamine B, *J. Phys. Chem. Solids*, 113(2018), p. 86.

[18] D.P. Dutta, A. Ballal, S. Chopade, and A. Kumar, A study on the effect of transition metal (Ti⁴⁺, Mn²⁺, Cu²⁺ and Zn²⁺)-doping on visible light photocatalytic activity of Bi₂MoO₆ nanorods, *J. Photochem. Photobiol. A*, 346(2017), p. 105.

[19] B. Xu, H. Yang, Q.T. Zhang, *et al.*, Design and Synthesis of Sm, Y, La and Nd-doped CeO₂ with a broom-like hierarchical structure: a photocatalyst with enhanced oxidation performance, *ChemCatChem*, 12(2020), p. 2638.

[20] A.S. Weber, A.M. Grady, and R.T. Koodali, Lanthanide modified semiconductor photocatalysts, *Catal. Sci. Technol.*, 2(2012), No. 4, p. 683.

[21] X.T. Xu, Y.X. Ge, B. Li, F.L. Fan, and F. Wang, Shape evolution of Eu-doped Bi₂WO₆ and their photocatalytic properties, *Mater. Res. Bull.*, 59(2014), p. 329.

[22] Z.Y. Jiang, Y.Y. Liu, T. Jing, *et al.*, Enhancing the photocatalytic activity of BiVO₄ for oxygen evolution by Ce doping: Ce³⁺ ions as hole traps, *J. Phys. Chem. C*, 120(2016), No. 4, p. 2058.

[23] B. Xu, Q.T. Zhang, S.S. Yuan, M. Zhang, and T. Ohno, Synthesis and photocatalytic performance of yttrium-doped CeO₂ with a porous broom-like hierarchical structure, *Appl. Catal. B*, 183(2016), p. 361.

[24] D.Y. Liang, Y. Ding, N. Wang, *et al.*, Solid-state reaction synthesis for mixed-phase Eu³⁺-doped bismuth molybdate and its luminescence properties, *Mod. Phys. Lett. B*, 31(2017), No. 26, art. No. 1750241.

[25] Q. Hao, F.H. Du, T. Xu, *et al.*, Evaluation of Nb-Doping on performance of LiNiO₂ in wide temperature range, *J. Electroanal. Chem.*, 907(2022), art. No. 116034.

[26] J.L. Yuan, X.Y. Zeng, J.T. Zhao, Z.J. Zhang, H.H. Chen, and X.X. Yang, Energy transfer mechanisms in Tb³⁺, Yb³⁺ codoped Y₂O₃ downconversion phosphor, *J. Phys. D: Appl. Phys.*, 41(2008), No. 10, art. No. 105406.

[27] L.Y. Zhou, J.X. Shi, and M.L. Gong, Synthesis and photoluminescence properties of SrLu₂O₄:Eu³⁺ superfine phosphor, *Mater. Res. Bull.*, 40(2005), No. 10, p. 1832.

[28] H.D. Li, W.J. Li, S.N. Gu, F.Z. Wang, X.T. Liu, and C.J. Ren, Forming oxygen vacancies inside in lutetium-doped Bi₂MoO₆ nanosheets for enhanced visible-light photocatalytic activity,

*Mol. Catal.*, 433(2017), p. 301.

[29] W. Liu, X.G. Lu, R.H. Ouyang, and W.S. Zheng, Size, electronic and magnetic effects on the deviation of Retgers' law in binary FCC alloys, *J. Solid State Chem.*, 316(2022), art. No. 123569.

[30] D.J. Hou, X.X. Pan, J.Y. Li, W.J. Zhou, and X.Y. Ye, Structure and luminescence properties of Sm³⁺ doped Y₂MoO₆ phosphor under near ultraviolet light excitation, *J. Rare Earths*, 35(2017), No. 4, p. 335.

[31] H.D. Li, W.J. Li, X.T. Liu, C.J. Ren, X. Miao, and X.Y. Li, Engineering of Gd/Er/Lu-triple-doped Bi₂MoO₆ to synergistically boost the photocatalytic performance in three different aspects: Oxidizability, light absorption and charge separation, *Appl. Surf. Sci.*, 463(2019), p. 556.

[32] H.D. Li, W.J. Li, F.Z. Wang, X.T. Liu, and C.J. Ren, Fabrication of two lanthanides co-doped Bi₂MoO₆ photocatalyst: Selection, design and mechanism of Ln₁/Ln₂ redox couple for enhancing photocatalytic activity, *Appl. Catal. B*, 217(2017), p. 378.

[33] H.D. Li, W.J. Li, S.N. Gu, F.Z. Wang, and H.L. Zhou, In-built Tb⁴⁺/Tb³⁺ redox centers in terbium-doped bismuth molybdate nanograss for enhanced photocatalytic activity, *Catal. Sci. Technol.*, 6(2016), No. 10, p. 3510.

[34] L.W. Zhang, T.G. Xu, X. Zhao, and Y.F. Zhu, Controllable synthesis of Bi₂MoO₆ and effect of morphology and variation in local structure on photocatalytic activities, *Appl. Catal. B*, 98(2010), No. 3-4, p. 138.

[35] C.S. Guo, J. Xu, S.F. Wang, L. Li, Y. Zhang, and X.C. Li, Facile synthesis and photocatalytic application of hierarchical mesoporous Bi₂MoO₆ nanosheet-based microspheres, *CrystEngComm*, 14(2012), No. 10, p. 3602.

[36] Z.J. Zhang, W.Z. Wang, E.P. Gao, M. Shang, and J.H. Xu, Enhanced photocatalytic activity of Bi₂WO₆ with oxygen vacancies by zirconium doping, *J. Hazard. Mater.*, 196(2011), p. 255.

[37] G. Liu, H.G. Yang, X.W. Wang, *et al.*, Enhanced photoactivity of oxygen-deficient anatase TiO₂ sheets with dominant{001}facets, *J. Phys. Chem. C*, 113(2009), No. 52, p. 21784.

[38] S. Usai, S. Obregón, A.I. Becerro, and G. Colón, Monoclinic–tetragonal heterostructured BiVO₄ by yttrium doping with improved photocatalytic activity, *J. Phys. Chem. C*, 117(2013), No. 46, p. 24479.

[39] T. Gougousi and Z.Y. Chen, Deposition of yttrium oxide thin films in supercritical carbon dioxide, *Thin Solid Films*, 516(2008), No. 18, p. 6197.

[40] X.H. Ma, W.J. Li, C.J. Ren, *et al.*, A novel noble-metal-free binary and ternary In₂S₃ photocatalyst with WC and "W-Mo auxiliary pairs" for highly-efficient visible-light hydrogen evolution, *J. Alloys Compd.*, 875(2021), art. No. 160058.

[41] Y.Y. Wu, H.D. Ji, Q.M. Liu, *et al.*, Visible light photocatalytic degradation of sulfanilamide enhanced by Mo doping of BiOBr nanoflowers, *J. Hazard. Mater.*, 424(2022), art. No. 127563.

[42] P. Franco, W. Navarra, O. Sacco, *et al.*, Photocatalytic degradation of atrazine under visible light using Gd-doped ZnO prepared by supercritical antisolvent precipitation route, *Catal. Today*, 397-399(2022), p. 240.

[43] V. Arun, V. Manikandan, M. Alsalhi, *et al.*, An efficient optical properties of Sn doped ZnO/CdS based solar light driven nanocomposites for enhanced photocatalytic degradation applications, *Chemosphere*, 300(2022), art. No. 134460.

[44] X.H. Ma, C.J. Ren, H.D. Li, *et al.*, A novel noble-metal-free Mo₂C–In₂S₃ heterojunction photocatalyst with efficient charge separation for enhanced photocatalytic H₂ evolution under visible light, *J. Colloid Interface Sci.*, 582(2021), p. 488.

[45] X.H. Ma, W.J. Li, H.D. Li, *et al.*, Fabrication of novel and noble-metal-free MoP/In₂S₃ Schottky heterojunction photocatalyst with efficient charge separation for enhanced photocatalytic H₂ evolution under visible light, *J. Colloid Interface Sci.*,

617(2022), p. 284.

[46] X.H. Ma, W.J. Li, C.J. Ren, *et al.*, Construction of novel noble-metal-free MoP/CdIn$_2$S$_4$ heterojunction photocatalysts: Effective carrier separation, accelerating dynamically H$_2$ release and increased active sites for enhanced photocatalytic H$_2$ evolution, *J. Colloid Interface Sci.*, 628(2022), p. 368.

[47] X.H. Ma, W.J. Li, C.J. Ren, *et al.*, Fabrication of novel noble-metal-free ZnIn$_2$S$_4$/WC Schottky junction heterojunction photocatalyst: Efficient charge separation, increased active sites and low hydrogen production overpotential for boosting visible-light H$_2$ evolution, *J. Alloys Compd.*, 901(2022), art. No. 163709.

[48] Q. Zhu, C.S. Xie, H.Y. Li, and Q.C. Yang, Comparative study of ZnO nanorod array and nanoparticle film in photoelectric response and charge storage, *J. Alloys Compd.*, 585(2014), p. 267.

[49] X.H. Ma, W.J. Li, C.J. Ren, *et al.*, Study of iron group transition metal phosphides (M$_2$P, M = Ni, Co, Fe) for boosting photocatalytic H$_2$ production, *Sep. Purif. Technol.*, 316(2023), p. 123805.

[50] R.Q. Yang, N. Liang, X.Y. Chen, *et al.*, Sn/Sn$_3$O$_{4-x}$ heterostructure rich in oxygen vacancies with enhanced visible light photocatalytic oxidation performance, *Int. J. Miner. Metall. Mater.*, 28(2021), No. 1, p. 150.

[51] T.T. Qin, X.Y. Zhang, D. Wang, *et al.*, Oxygen vacancies boost δ-Bi$_2$O$_3$ as a high-performance electrode for rechargeable aqueous batteries, *ACS Appl. Mater. Interfaces*, 11(2019), No. 2, p. 2103.

[52] Y.J. Sun, H. Wang, Q. Xing, *et al.*, The pivotal effects of oxygen vacancy on Bi$_2$MoO$_6$: Promoted visible light photocatalytic activity and reaction mechanism, *Chin. J. Catal.*, 40(2019), No. 5, p. 647.

[53] L. Hao, H.N. Zhang, J.C. Yan, L.J. Cheng, S.J. Guan, and Y. Lu, Effect of oxygen vacancy on photocatalytic activity and relevant mechanism, *J. Tianjin Univ. Sci. Technol.*, 33(2018), No. 5, p. 1.

[54] H.D. Li, W.J. Li, X.T. Liu, C.J. Ren, F.Z. Wang, and X. Miao, Fabrication of bismuth molybdate photocatalyst co-substituted by gadolinium and tungsten for bismuth and molybdenum: Design and radical regulating by the synergistic effect of redox centers and oxygen vacancies for boosting photocatalytic activity, *J. Taiwan Inst. Chem. Eng.*, 89(2018), p. 86.

[55] D. Zhang, M.Q. Wu, J.Y. Hao, *et al.*, Construction of Z-scheme heterojunction by coupling Bi$_2$Sn$_2$O$_7$ and BiOBr with abundant oxygen vacancies: Enhanced photodegradation performance and mechanism insight, *J. Colloid Interface Sci.*, 612(2022), p. 550.